

Exploring magmatic gas and subvolcanic hydrothermal system interactions: Mineralogy and sulfur isotope characteristics of the Holocene volcanic products at Mt. Tangkuban Parahu, Indonesia.

Syahreza Saidina Angkasa (✉ syahreza.s.a@gmail.com)

Universitas Pertamina <https://orcid.org/0000-0001-6264-5929>

Ohba Tsukasa

Akita University: Akita Daigaku

Imura Takumi

Yamagata University: Yamagata Daigaku

Pearlyn Manalo

Akita University: Akita Daigaku

Takahashi Ryohei

Akita University: Akita Daigaku

Full paper

Keywords: subvolcanic-hydrothermal system, magmatic-hydrothermal interaction, steam-blast eruption, volcanic ash, sulfur isotopes

Posted Date: January 12th, 2021

DOI: <https://doi.org/10.21203/rs.3.rs-141850/v1>

License:  This work is licensed under a Creative Commons Attribution 4.0 International License.

[Read Full License](#)

Abstract

A subvolcanic-hydrothermal system involves complex interaction between magma, magmatic fluids, and hydrothermal system at stratovolcanoes in subduction setting. These interactions are responsible for magmatic-hydrothermal eruption associated with rapid injection of magmatic gas into hydrothermal system at a certain depth of volcanic edifice. However, capturing these interactions is challenging due to inaccessibility to the crater conduit within the edifice. Therefore, we selected a method to analyze the volcanic products from several episodic phreatic and phreatomagmatic eruptions during the Holocene at Tangkuban Parahu, Indonesia. In this context, Holocene volcanic products are one of the best examples to understand an interplay between magma, magmatic fluids, and hydrothermal system in producing violent eruptions. In this study, we carried out petrological and sulfur isotope analysis only for the hydrothermally altered lithic ash particles, a part of proximal volcanic products. Mineral assemblages mostly exhibit a typical acid-sulfate and advanced argillic alteration, consisting of alunite, kaolinite, and silica minerals. Acid-sulfate and advanced argillic alteration indicates that those mineral assemblages were formed under the formation temperature ranging from ~100 to ~260 . The calculated temperature from sulfur isotopic fractionation of sulfate-sulfide shows 230-240 , which is almost identical with assigned temperature from mineral assemblages. Sulfur isotope and jarosite occurrence indicate the supergene alteration associated with oxygen entrainment to the hydrothermal system that oxidize pyrite to jarosite. Sulfur isotopic variation throughout the studied stratigraphy represents influx of magmatic gas to the hydrothermal system. Moreover, zoned P-bearing alunite represents repetitive injection of magmatic gas to the active acidic hydrothermal system, which also indicates the magmatic-hydrothermal interaction below the crater. Occurrence of enargite and chalcopyrite represents the nature of upper-level high sulfidation system at shallow volcanic edifice of the Tangkuban Parahu volcano. Furthermore, we showed that coupled petrological and sulfur isotope analysis has paramount importance to evaluate the conditions of the subvolcanic hydrothermal system, magmatic-hydrothermal interaction, and the origin of steam-blast eruptions at volcanoes that contain subvolcanic-hydrothermal systems.

Introduction

A subvolcanic-hydrothermal system involves complex interactions between magma, magmatic fluid, and hydrothermal fluid at high-terrain stratovolcanoes in subduction settings (Hedenquist and Lowernstern, 1994). A hydrothermal system is responsible for a magmatic-hydrothermal eruption associated with a rapid injection of magmatic gas into the hydrothermal system from magmatic intrusion at a certain depth of volcanic edifice (Mastin et al., 1995; Browne and Lawless, 2000; Stix and Moore, 2018). The magma-hydrothermal interaction leads fragmentation of various rocks along the conduits in the stratovolcano, including cognate magmatic rocks and hydrothermally altered country rocks (Browne and Lawless, 2001; Ohba and Kitade, 2005; Ohba et al., 2009). As a result, the volcanic products of the eruption are highly diverse in component (e.g., Ohba and Kitade, 2005; Pardo et al., 2014). The diversity of the components provides an opportunity to understand the dynamics of the subvolcanic- and magmatic-hydrothermal

systems (e.g., Hedenquist and Henley, 1985; Ohba and Kitade, 2005; Ohba et al., 2007; Minami et al., 2016) as well as the contribution of magmatic activities resulting in violent eruptions.

A crucial question is how the mineralogy in subvolcanic-hydrothermal system varies by the interaction with magmatic components along the active volcanic conduit. Answering this question is challenging because of the inaccessibility to the underground system within the volcanic edifice. Chemical and physical variations in volcanic-hydrothermal system can be recorded as mineralogical characteristics in eruptive products (e.g., Ohba and Kitade, 2005; Ohba et al., 2007; Takahashi and Yahata, 2018). The eruptive products frequently preserve the assemblages from hydrothermal mineral zones (e.g., John et al., 2008; Minami et al., 2016; Imura et al., 2019) which are similar to those developed in ancient hydrothermal ore deposits (e.g., Hedenquist and Lowernstern, 1994; Sillitoe, 2010). In addition to the similarity to the ancient hydrothermal systems, volcanic products can provide information of on-going interaction between magma and the hydrothermal system (e.g., Miyagi et al., 2020).

Sulfur is one of important elements in sub-volcanic hydrothermal systems. Sulfur species in volcanic gas derived from magma can mix with ground water to make sulfuric acid that promotes chemical reactions between the fluid and rocks (e.g., Sakai, 1968; Giggenbach, 1997; Landis and Rye, 2005). To understand magma-hydrothermal interactions under a volcano based on observations on volcanic products, sulfur-bearing minerals should be carefully examined. Sulfur isotope analysis of the minerals is a potential prime method to understand the magma-hydrothermal interactions (e.g., Imai et al., 2007; Zimbelman et al., 2005; Ikehata and Maruoka, 2016, 2019). Therefore, we apply the sulfur isotopic analysis to the volcanic products which are derived from magma-hydrothermal interactions.

The present work focused on volcanic products from the proximal area of Tangkuban Parahu volcano, Indonesia, which has an established tephra-stratigraphy (cf. Angkasa et al., 2019). The volcano has been active within the Holocene epoch. During Holocene, the activities are magmatic-hydrothermal and phreatic explosive eruptions, along with several magmatic intrusion in contact with water bodies (e.g., crater lake) to explode as a common phreatomagmatic eruption (CVGHM, 2016; Angkasa et al., 2019). In this context, Holocene volcanic products from this volcano are good examples to understand interactions between magma and a hydrothermal system. In this study, we carried out petrological observation on ash particles to document hydrothermal mineral assemblage and overprinting relationship (e.g., veinlets, alteration type) referring the fossil and active geothermal systems at the stratovolcanoes worldwide (e.g., Hedenquist and Henley, 1985; Wohletz and Heiken, 1992; Hedenquist and Taran, 2013). We also performed sulfur isotopic analysis to understand formation conditions of sulfate and sulfide, contribution of magma to the eruptions, and magma-hydrothermal interaction in the subvolcanic hydrothermal system.

Geological setting

Tangkuban Parahu is an active basaltic to andesitic stratovolcano, located in West Java, Indonesia (Figs. 1A and B). The volcano had experienced two main caldera-forming eruptions at ca. 500 ka and ca. 100

ka (Kartadinata, 2005). Repetitive effusions of a vast amount of lava flows at ca. 180 ka (Sunardi and Kimura, 1998) had also occurred before the formation of the present volcanic edifice of Tangkuban Parahu within the prominent arcuate of Sunda Caldera (Nasution et al., 2004).

Historical eruptions at Tangkuban Parahu were documented in 1929, 1961, 1969, 1971, 1983, 1986, 1992, 2004, and 2013 (Kusumadinata, 1976; CVGHM, 2016), and recently in 2019 (www.magma.vsi.go.id). Most of the eruptions are relatively small-scale explosion associated with phreatomagmatic and phreatic or hydrothermal activities (Kartadinata et al., 2005; CVGM, 2016; Angkasa et al., 2019). The distribution of Holocene volcanic products is limited in about 1-1.5 kilometers around the craters (Angkasa et al., 2019).

Holocene volcanic activities

Holocene volcanic activities of Tangkuban Parahu are mostly still understudied in the sense of the eruption process as well as the characteristic of volcanic products. The Holocene eruptive products are composed of fine-coarse fall-out and base surge deposits (Kartadinata et al., 2002; Angkasa et al., 2019), which covered a total of 20 km² area of the summit area of Tangkuban Parahu volcano (CVGHM, 2016). The volcanic products consist of various proportions of lithics, magmatic juveniles, and isolated free crystals in the tephra layers from several episodic eruptions (Angkasa et al., 2019). Although the phreatic explosion is thought to be a predominant eruption type during the Holocene epoch (Kartadinata et al., 2002), the recent observation of ash components suggests the occurrence of several phreatomagmatic pulses within the 10,000 years (Angkasa et al., 2019), indicating a vital role of the magmatic intrusion and degassing in producing the explosion during the Holocene epoch.

Hydrothermal activities

The Tangkuban Parahu geothermal system widely extends to Ciater, Maribaya, and Batugede which is one of the most extensive geothermal systems associated with volcanic-magmatic activities among West Java, Indonesia (Hochstein and Sudarman, 2015). Hydrothermal manifestation currently develops as active fumaroles, hot springs, and solfataras with a fumarolic temperature of 90-100 °C (Sriwarno, 1984; Saputra and Suryantini, 2015). At Ratu Crater, the temperature of fumaroles occasionally increased higher than 300 °C in 1952, 1961, and 1969 (Suryo, 1981 and 1985). Hydrothermal alteration covered the area of ~1 km² (Fig. 1B, C, and D), scattered close to the proximity of Ratu Crater. Hydrothermal alteration minerals consist of a zonation of silica and native sulfur at Ratu, Upas, and Baru Craters (Fig. 1C), whereas silica and native sulfur occur together with pyrite at Domas Crater (Saputra and Suryantini, 2015).

Methods

Sampling and sample preparation

Volcanic products were sampled during the fieldwork campaign in August 2017 and October 2018 (Fig. 2A, B, and C). More than 50 samples were collected from several outcrops at the proximal area of the Tangkuban Parahu volcano (Fig. 1B). Most of the volcanic products are white and yellow to reddish in color at a wet condition. We cleaned the outcrops to avoid contamination from surrounding organic material. From the outcrop, volcanic products were carefully collected in the field by using a small shovel and placed into a plastic container. A total of 26 representative samples (Fig. 2) were manually sieved into different fractions. For this study, we selected volcanic products with a size of particles smaller than 500 micrometers (μm). Selected particles were bathed with distilled water along with an ultrasonic cleaner to remove clay and dust from the samples and dried with an oven at 40 °C for 12 hours.

X-ray diffraction

X-ray diffraction (XRD) analysis was performed to identify hydrothermal and magmatic mineral phases in the volcanic products on a total of 21 sieved samples. Volcanic products were manually crushed into a fine-grained powder using iron and agate mills. Powder samples were used to produce randomly oriented and oriented samples. Ethylene glycol treatment was optionally applied to some of the oriented samples to verify the presence of 15 Å-smectite group minerals. The XRD instrument was a Rigaku Multi-Flex installed at Faculty of International Resource Sciences, Akita University. The operation conditions are at 30 kV and 16 mA, using Cu target anode for CuK α radiation source. Randomly oriented samples were scanned with a step width of 0.01 and a counting time of 1 min⁻¹, whereas the oriented samples were scanned with a step width of 0.02 and a counting time of 0.5 min⁻¹. Moreover, synthetic quartz was analyzed for optimization of X-ray intensity.

Optical and electron microscopes

A total of 15 thin and polished sections from different ash layers (Fig. 2) was observed under optical and electron microscopes, using a Nikon ECLIPSE LV100N and a JEOL JSM-IT300 scanning electron microscope (SEM) equipped with energy dispersive spectrometer (EDS, an Oxford instrument Inca X-act). Microprobe analysis was operated at an accelerating voltage of 15 kV, a beam current 2.2 nA, and a working distance 10 mm. Cobalt was analyzed for an optimization of X-ray intensity. To avoid sample damage, we applied different live times during microprobe analysis of hydrothermal and magmatic minerals. Silica and magmatic minerals (e.g., plagioclase, augite, Fe-Ti oxide) were analyzed at the live time for 80 s. Alunite and kaolinite were analyzed at the live time of 30 s.

Most of the minerals were determined based on their general stoichiometry acquired from EDS spot chemical analysis. Alunite ((K, Na, Ca) Al₃(SO₄)₂(OH)₆) and kaolinite (Al₂Si₂O₇(OH)₂) were evaluated by the general formula of DG₃(TX₄)₂X₆ (Bayliss et al., 2010) and X₄Z₄O₁₀(OH)₈ with a total oxygen number of 11 and 7, respectively. Moreover, pristine Si-Al clay mineral (kaolinite) was evaluated by using Al/Si ratio of kaolinite stoichiometry close to ~1 because kaolinite commonly occur as fine crystal aggregates and interlocked together with silica minerals.

Raman spectroscopy

Raman spectroscopy analysis using a Renishaw Invia Raman Microspectrometer at Faculty of International Resource Sciences, Akita University was performed to determine some phases (silica and Ti-oxide polymorph minerals). Silica minerals are specified after a near-pure SiO₂ phase is identified with EDS, except for pristine quartz crystals. The same method is applied to Ti-oxide minerals to distinguish rutile and anatase. We operated at a laser power of 150 mW and a slit diameter of 1 μm, and an argon excitation laser of 532 nm-1. Silica standard was employed to calibrate the Raman spectrum. A CrystalSleuth software (Laetsch and Down, 2006) was employed to correlate the Raman spectra with specific crystal reference in the American Mineralogist Crystal Structure Database (www.ruff.info).

Sulfur isotopes

Sulfur isotope analysis was performed to constrain the formation conditions of the sulfate and sulfide minerals. A total of 21 samples was handpicked from different tephra layers to produce the temporal variation of the sulfur isotopic composition of volcanic products. Alunite crystals were handpicked from the ash particle of $1 \leq \leq 2$ in size and collected from yellow and pinkish ash particles, according to macroscopic detailed characteristics alunite bearing hydrothermally altered rocks (Rye, 1993). Jarosite was sampled from a highly oxidized tephra layer in Unit 8 (Fig. 2C). Pyrite in silica-rich ash particles was extracted from gently crushed ash particles because isolated pyrite crystal is absent from the volcanic products. In addition, XRD analysis was performed for all samples to confirm the presence of sulfate and sulfide minerals.

Sulfur in alunite and jarosite were dissolved with 0.5 N NaOH at 80 °C (Wesserman et al., 1992; Manalo et al., 2018), whereas pyrite was decomposed with 16 N HNO₃ and Br₂ solutions at 90 °C. Leached sulfur solutions were extracted as BaSO₄ precipitates by adding 10% BaCl₂ · 2H₂O. The BaSO₄ precipitates were packed with V₂O₅ in tin foils (modified from Yanagisawa and Sakai, 1983). Sulfur isotope measurements were performed with a mass spectrometer (Thermo Fisher Scientific Delta V at Faculty International Resource Science, Akita University). Seawater sulfate (NBS-127) and barium sulfate (SO-5 and SO-6) were employed as standards, which were provided by the International Atomic Energy Agency (IAEA). The isotopic ratios are presented with an expression of δ³⁴S per mil (‰) relative to the sulfur concentration of Troilite in Canyon Diablo Meteorite. The precision of analysis is better than ±0.2 ‰.

Results

Mineral phase identification

X-ray diffractogram and a summary of identified mineral phases are presented in Figures 3 and 4, respectively. Most of the X-ray spectrums indicate the occurrence of quartz, cristobalite, and tridymite as dominant phases in all analyzed samples. These minerals occur together with alunite, 7Å kaolin mineral, and anatase. However, 7Å kaolin mineral and anatase are not necessarily contained in the volcanic

products. Although the spectrums of 7Å kaolin were carefully examined, there is no indication of dickite (Fig. 4). It is noteworthy that 15 Å-smectite group minerals are absent. Major magmatic minerals are sanidine, plagioclase, and augite. Orthopyroxene randomly occurs at the middle and upper portion of composite stratigraphy (Fig. 4). The XRD spectrums also indicate the presence of jarosite and goethite in several tephra layers.

Volcanic ash petrography

Total petrographic observation indicates the abundance of altered ash particles ($n = 351$ ash particles, $_{\text{observation}} = 23$ ash particles/sample). From the petrographic observation, ash particles can be categorized into two types of hydrothermally altered ash particles and unaltered pyroclasts. The hydrothermally altered ash particles are classified into two: 1) partly altered glassy pyroclasts and 2) intensely altered ash particles. Here, we focus on detailed petrographic observation of the hydrothermally altered ash particles. In this section, we will describe the petrography focusing on the mineral assemblages and textural variation of hydrothermally altered lithic ash particles.

Partly altered glassy pyroclasts

Some of highly vesicular glassy ash particles are partly altered (Fig. 5A). Magmatic minerals are composed of micro-phenocryst of plagioclase ($\text{An}_{54-58}\text{Or}_{01-03}\text{Ab}_{39-43}$), pigeonite ($\text{En}_{37}\text{Wo}_{09}\text{Fs}_{53}$), and Fe-Ti oxide crystals which occur as euhedral crystals with sizes of $<10 \mu\text{m}$. Volcanic glass occurs in the groundmass. A BSE image shows a local alteration in groundmass, which occurs as colloform-like banding (Dong, 1995) contacting embedded hydrothermally altered lithics (Fig. 5A and B).

Intensely altered lithics

In the intensely altered lithics, the phenocrysts and microlites of magmatic minerals and the glassy groundmass are intensely altered. There are two main hydrothermal mineral assemblages in the intensely altered ash particles (Fig. 4). The association of alunite alteration represents the most abundant alteration type, with approximately 57% of observed ash particles. It is associated with several hydrothermal minerals, including opal, cristobalite, quartz, kaolinite, and jarosite. Quartz alteration is the second abundant alteration type, about 30% of the total petrographic observation, which occurs with ore minerals. Furthermore, these two hydrothermal mineral associations are further subclassified into the following five specific alteration types and two veinlet feeders.

Opal alteration

Opal alteration was identified in many vesiculated ash particles (Figs 6A, B, and D). Opal shows prominent Raman peaks at 267, 508, 561, and 782 cm^{-1} (Fig. 6C). Pseudomorph textures indicate the replacement of opal after clinopyroxene ($\text{En}_{35}\text{Wo}_{34}\text{Fs}_{29}$) and plagioclase ($\text{An}_{47}\text{Or}_{04}\text{Ab}_{49}$). The remnants of magmatic minerals, together with unaltered clinopyroxene (augite) and Fe-Ti oxide, suggest that alteration is moderate in intensities.

Opal-cristobalite+alunite±kaolinite alteration

Opal-cristobalite-alunite±kaolinite alteration was found in angular and dense ash particles (Figs. 6D and E), where vesicular textures are absent. Opal is commonly associated with cristobalite, replacing magmatic minerals. Cristobalite occurs as a cluster of nearly-equant fine-grained (<1 µm) crystals. Pristine cristobalite displays Raman peaks at 226 and 411 cm⁻¹ (Fig. 6C). Altered groundmass consists of alunite, kaolinite, anatase, and mixture of silica minerals. In Figure 6E, the same mineral assemblage appears in angular and dense ash particles, although it shows different occurrence. In these particles, opal, cristobalite, and alunite have entirely replaced the plagioclase crystal. Alunite occurs as zoned crystals with >50 µm in diameters, which commonly associated with kaolinite.

Quartz-alunite±kaolinite alteration

Quartz-alunite±kaolinite alteration (Figs. 7A and B) was predominantly observed in a subrounded to rounded ash particles. Quartz occurs as subhedral to euhedral fine-grained crystals, which are associated with the alunite crystals. Alunite occurs as euhedral, bladed-lath, and zoned crystals. The crystals range from 5 to 10 µm in diameter. Most of the alunite have an intermediate composition between $KAl_3(SO_4)_2(OH)_6$ and $NaAl_3(SO_4)_2(OH)_6$. Huangite (Li et al., 1992) are found in quartz-rich ash particles as fine-grained anhedral crystals, containing anatase, pyrite, and chalcopyrite. Kaolinite commonly occurs as circular crystal clusters and fine-grained alteration groundmass.

Alunite-jarosite alteration

Alunite-jarosite alteration was observed in highly porous ash particles, where the voids or pore zones mostly occupied by a mixture of silica minerals and anatase crystals (Fig. 7C). Jarosite is dominant in the alunite-jarosite intergrowth. Alunite occurs as subhedral to euhedral crystal with >10 µm in size, whereas jarosite mostly shows anhedral crystals, ranges from 10-20 µm in diameter.

Quartz alteration

Quartz alteration was observed in angular to subangular ash particles (Figs. 7D and 7E). Dissolution vugs are the most common texture of the quartz alteration. Quartz occupies 90-95 vol% of ash particles, indicating pervasive alteration intensities. Quartz occurs as euhedral, equant crystals with almost pure SiO₂ concentration (98-100 wt.%); such crystals commonly form an interlocked mosaic cluster (Fig. 7D). Crystals vary in size, ranging from 10 to 50 µm. Quartz alteration is associated with magnetite, titanomagnetite, enargite, chalcopyrite (Figs. 7E and 9A), and pyrite. These minerals disseminate throughout the ash surface with a total concentration of <1 vol%, occurring as pore or vug filling minerals.

Alunite-kaolinite-goethite±silica veinlet

Silica-alunite-kaolinite-goethite veinlet was identified in a holocrystalline-equigranular ash particle (Fig. 8A and B). The host rock mineralogy consists of quartz, sanidine, ilmenite, and sanidine. Most of the minerals are resistant to hydrothermal alteration, except for sanidine (An₀₄Or₅₆₋₇₄Ab₂₂₋₄₀) which

underwent alunite alteration. The veinlet has a thickness of ~50 μm , occupying approximately 25% ash particle surface. Veinlet mineralogy consists of silica, anatase, kaolinite, goethite, P-bearing alunite, and Na-K alunite. P-bearing alunite and anatase commonly occur as crystal inclusions in Na-K alunite veinlets. Kaolinite-goethite shows an intergrowth texture, which moderately replaced Na-K alunite (Fig. 8B).

Quartz-pyrite veinlet

A quartz-pyrite veinlet was observed in the alunite vein of a porphyritic ash particle (Figs. 8C and 8D). Host rock is possibly an extremely silicified volcanic rock. The alunite vein is mainly composed of Na-K alunite and P-bearing alunite. Within the alunite vein, a 15-20- μm -thick quartz-pyrite veinlet is developed. Pyrite occurs as centerline crystal inclusions of pyrite in quartz crystals (Fig. 8D). Quartz in the veinlets displays a uniform band in the BSE image, indicating homogenous SiO_2 concentration in the veinlets. Selvages are primarily composed of fine-grained crystal of quartz and P-bearing alunite. The presence selvages indicate the relative timing of quartz-pyrite veinlet deposition after the alunite vein (Fig. 8D), which also provides an evidence of hydrothermal alteration overprint.

Sulfur isotopes

Sulfur isotopic compositions of sulfide and sulfate minerals are presented in Table 2. The $\delta^{34}\text{S}$ values of alunite are isotopically heavier compare to pyrite and jarosite, widely range from +2.8 to +20.8 ‰ (n:19). The $\delta^{34}\text{S}$ values of pyrite and jarosite were only measured in Tangkuban Parahu Tephra (TPT) 4 and 8, respectively. Pyrite in TPT 4 (Tangkuba Parahu-TP 15) has lighter $\delta^{34}\text{S}$ values (-2.7‰ and -3.5‰) than those of alunite. Jarosite yielded a $\delta^{34}\text{S}$ value of -1.6 ‰, which is close to that of pyrite.

The $\delta^{34}\text{S}$ values of all sulfur-bearing minerals were plotted against the stratigraphic unit of proximal volcanic products to represent the temporal change of the sulfur isotopic composition (Fig. 10). The $\delta^{34}\text{S}$ values of alunite in the lower stratigraphy show the range between +5 to +10‰ (TPT 4, 3, 2, and 1). On the other hand, those in upper stratigraphy are lighter in the upper stratigraphy and concentrated approximately in +5‰ (TPT 6, 7, and 10). Moreover, the decreasing upward trend of the alunite $\delta^{34}\text{S}$ is illustrated even within a single unit of TPT4. The trend shows the temporal change from +10‰ in TP17 lowermost to +5‰ in TP11 uppermost.

Discussion

Hydrothermal alteration

Some alteration types were identified from the mineralogical observations on the volcanic products as described above. Silica, alunite alterations are the major alterations and some minor alteration types were inferred from the presence of sulfide, sulfosalt, jarosite, and goethite.

Cristobalite, opal, tridymite, and quartz are identified from the volcanic products. Cristobalite and opal commonly precipitate under low pressure and temperature, probably formed at a temperature range from 100 to 150 °C (Fournier, 1985). The silica minerals constitute the silica alteration caused by cation leaching and dissolution of the magmatic components by acidic fluids (Christenson et al., 2010, Rodriguez and van Bergen, 2017). Si, Al, and Ti are resilient during the cation-leaching process (Nogami and Yoshida, 1993, 1995; Hara and Tsuchiya, 2009).

Quartz occurs pervasively in silicified ash particles (Figs. 7A, D, and E). It commonly crystallizes at a relatively high temperature (>180 °C) in the hydrothermal environment, depending on the silica solubility in hydrothermal fluids (Fournier, 1985; Rimstidt, 1987). The coexistence of quartz and kaolinite in ash particles (Figs. 7B, D, and E) can constrain the crystallization temperature, by the following reaction of the Al₂O₃-SiO₂-H₂O system (Hemley et al., 1980; Chatterjee et al., 1984) :



The reaction is equilibrium at a temperature range 260-280 °C. Pyrophyllite and other high temperature minerals (diaspore, andalusite) are absent from the ash particles, indicating the formation temperature of the quartz and kaolinite are lower than 260 °C.

Alunite is the most abundant sulfur-bearing mineral, which is associated with silica minerals. Alunite and P-bearing alunite are the most common alunite species in the volcanic products. The P-bearing alunite and associated alunite (Figs. 8A and D) were possibly influenced by magmatic components at hypogene environment because phosphate in alunite is related to phosphorous released from magmatic apatite (Stoffregen and Alpers, 1987). The zoned alunite with P-rich zone in the veinlets implies pulses of magmatic components into the acidic hydrothermal environment.

Jarosite is associated with goethite and alunite-jarosite intergrowth (Figs. 4 and 7C), which is mostly interpreted as pyrite-alunite intergrowth in origin (Rye et al., 1992; Watanabe et al., 1997). The similarity in sulfur isotopic composition suggests that the jarosite was formed by the oxidation of pyrite (e.g., Rye et al., 1992).

Sulfur isotope variation in alunite

Temporal variation

Heterogeneity of sulfur isotopic composition is clearly shown in alunite from this studied samples. The variation of sulfur isotopic composition for alunite reasonably suggests that the volcanic products contain various alunite minerals formed at different stages and conditions. In volcanic environments, the variations of the sulfur isotopic composition are caused mainly by SO₂ disproportionation (Imai et al., 2007; Ikehata and Maruoka, 2016, 2019). During this hydration process of magmatic SO₂ gas, ³⁴S is predominantly partitioned into sulfate as SO₄²⁻, whereas representative S²⁻ as sulfide or H₂S depletes in

^{34}S (Ohmoto and Rye, 1987; Ohmoto and Goldhaber, 1999; Zimbelman et al., 2005). Consequently, a pair of sulfates (e.g., heavier gypsum or anhydrite) and sulfide (e.g., lighter pyrite) can be formed in a magmatic-hydrothermal environment (Imai et al., 2010; Ikehata and Maruoka, 2016, 2019). In this study, only TP15 in TPT 4 shows a pair of alunite and pyrite and indicates a possibility of sulfate-sulfide equilibrium condition (Ohmoto and Rye, 1987; Ohmoto and Goldhaber, 1997). Therefore, a pair of isotopically heavy alunite (+20 ‰) and light pyrite (-5 ‰) in TP15 of TPT 4 eruption implies the timing of development of an aqueous magmatic-hydrothermal system. In contrast with TP15 in TPT 4, most other samples contain only alunite as a sulfur mineral phase with a range of $\delta^{34}\text{S}$ from +5 to +10 ‰. This range indicates the SO_2 disproportionation had not proceeded enough to form the alunite-pyrite pair with the isotopic fractionation. This case is suitable at the oxidized stage of subvolcanic hydrothermal system with much abundance of magmatic SO_2 vapor (e.g., Satsuma-Iwojima in, Hendenquist and Taran, 2013). Moreover, after TPT 4, the sulfur isotopic compositions of alunite in the layers concentrate on 5 ‰ of $\delta^{34}\text{S}$, which is lighter than the values before TP11 of TPT 4. This stratigraphic variation of sulfur isotope might indicate an increase of input fluxes of magmatic vapor with their own isotopic composition (Fig. 10).

Sulfur isotope geothermometer

Sulfur isotope geothermometry (Ohmoto and Rye 1979, Ohmoto and Goldhaber, 1997) was applied for two pairs of sulfur isotopic compositions of alunite and pyrite from the TP15 in Unit 4, assuming the alunite and pyrite were in equilibrium (Table 1). The calculated equilibrium temperatures were 232 °C and 240 °C, respectively. The values are consistent with the temperatures estimated from the P-free alunite and the silica alteration (quartz and kaolinite). On the other hand, the P-bearing-alunite and huangite-alunite solid solution must have precipitated at higher temperatures. The zoned texture of alunite (Figs. 7B, 8A, and B) represents repeated injections of magmatic steam or gas (Aoki, 1991), which could result in the sulfur isotopic compositions similar to that of the magmatic steam or gas.

Comparison between Tangkuban Parahu and other volcanoes

We compared the $\delta^{34}\text{S}$ values of alunite with several available $\delta^{34}\text{S}$ datasets from Mt. Muine, Japan (Watanabe and Ohta, 2005), and Kawah Ijen, Indonesia (Scher et al., 2013) (Fig. 10). Watanabe and Ohta (2005) argued that the magmatic-steam or gas alunite has sulfur isotopic composition below +20 ‰, whereas the $\delta^{34}\text{S}$ values higher than +20 ‰ is falling into magmatic-hydrothermal alunite. At the Kawah Ijen, the alunite mostly shows sulfur isotopic composition within a range of +18 to +20 ‰ and classifies as magmatic-hydrothermal origin (Scher et al., 2013). These suggest that alunite in the Tangkuban Parahu volcanic products were mostly formed by the process of magmatic-steam or gas (Fig. 10). Nevertheless, a sample with the highest $\delta^{34}\text{S}$ value in TP15 of TPT4 is classified as magmatic-hydrothermal alunite.

Implication

Hydrothermal minerals in the volcanic products represent acid-sulfate or advanced argillic alteration (e.g., Arribas et al., 1995; Silitoe, 2010). Mineral assemblages represent the temperature conditions along the conduit. Cristobalite and opal alteration were formed at a temperature of 100-150 °C (Fournier, 1985) which is the temperature range in the near-surface condition below the crater (e.g., Lowernstern et al., 2018). Quartz-kaolinite alteration occurs at temperatures lower than 260 °C. The sulfur isotopic temperatures for the TPT15 are 232 and 240°C. These temperatures indicate that most of the ash particles were ejected from the hydrothermal system at temperatures below 300 °C. In addition, the presence of jarosite and goethite implies supergene alteration, indicating atmospheric oxygen entrainment to the hydrothermal system near the surface.

From the mineralogy of volcanic products, we can conclude that the alteration at the summit of Tangkuban Parahu volcano represents the nature of upper-level high sulfidation epithermal ore deposits (Hedenquist and Lowernstern, 1994; Arribas et al., 1995; Hedenquist et al., 1998). The occurrence of chalcopyrite and enargite in the volcanic product (Fig. 7E) is also the similarity to these ore systems. Tangkuban Parahu subvolcanic-hydrothermal system is similar to the models of volcanic-hydrothermal system in many high-terrains of calc-alkaline stratovolcanoes (e.g., Hedenquist and Lowernstern, 1994; Watanabe et al., 1997; Minami et al., 2016).

The stratigraphic sulfur isotopic variation implies increase in influx of magmatic vapor into the hydrothermal system. The abrupt increase in the vapor flux is consistent with the activity of magma at the TPT 4 when a series of phreatomagmatic eruptions occurred (Angkasa et al., 2019). Alunite-group minerals also indicate pulses of magmatic components into the hydrothermal system. This study showed that sulfur isotope of volcanic products is a useful method to detect the magmatic contribution on hydrothermal system.

Conclusions

In this work, the mineralogy and sulfur isotopic composition were observed and documented from the hydrothermally altered lithic ash particles, part of the Tangkuban Parahu proximal volcanic products. The followings are the conclusions:

1. Mineral assemblage exhibits a typical acid-sulfate and advanced argillic alteration with a temperature range from ~100 to ~260 °C, which is almost identical with the temperature of 230-240 °C calculated from the sulfate-sulfide ^{34}S fractionation equation.
2. The sulfur isotope and occurrence of jarosite indicate the supergene alteration associated with atmospheric oxygen entrainment to oxidize pyrite to jarosite.
3. Ore minerals such as enargite and chalcopyrite represent the nature of upper-level high sulfidation system at the shallow volcanic edifice.
4. Stratigraphic sulfur isotopic variation represents influx of magmatic gas into the hydrothermal system.

5. Sulfur isotope signature of the volcanic products has a paramount importance to evaluate the conditions of subvolcanic hydrothermal system, magmatic-hydrothermal interaction, and the origin of steam-blast eruptions at volcanoes that contain subvolcanic hydrothermal systems.

Declarations

Availability of data and materials

Not applicable

Competing interests

All authors declare that we have no competing interests.

Funding

SA are funded by Mobunkagakusho Japanese (MEXT) scholarship and the New Frontier Leading Program of JSPS. This work was also partially funded by JSPS Kankehi #17K1319 and #20K0524 (T.Ohba).

Authors' contributions

Conceptualization, SA; fieldwork, SA and TO; sample preparation, SA; XRD analysis, SA; Raman Spectroscopy analysis, SA, and TI; SEM-EDS, SA, TO, and TI; sulfur isotope preparation and analysis, SA, PM, and RT; manuscript, SA, TO, TI, and RT; funding acquisition, TO. All authors have agreed with the earlier version of the manuscript.

Acknowledgements

This paper is a part of the SA's doctoral thesis at Akita University, Japan. We thank Tangkuban Volcano Observatory staff (CVGHM) and the Indonesian Natural Conservation Centre (BKSDA) for their assistance in providing shelter during three fieldwork seasons at Tangkuban Parahu Volcano and sampling permit of volcanic products, respectively. Hinako Sato are acknowledged for her support during sulfur isotope analysis. Takuya Echigo are thanked for his support for the analysis of Raman Spectroscopy at Akita University, Akita, Japan. Yasushi Watanabe, Andrea Agangi, and Antonio Arribas are thanked for their constructive comments during the doctoral viva of SA, which was improved this manuscript.

References

Angkasa SS, Ohba T, Imura T, Setiawan I, Rosana MF (2019) Tephra-stratigraphy and Ash Componentry Studies of Proximal Volcanic Product at Mount Tangkuban Parahu, Indonesia: An Insight to Holocene Volcanic Activity. *Indonesian Journal on Geoscience*. doi: 10.17014/ijog.6.3.235-253.

Arribas Jr A, Cunningham CG, Rytuba JJ, Rye RO, Kelly WC, Podwyssocki MH, McKee EH, Tosdal RM (1995) Geology, geochemistry, fluid inclusions and isotope geochemistry of the Rodalquilar gold alunite deposit, Spain. *Economic Geology*. 90:795-822.

Aoki M (1991) Mineralogical features and genesis of Alunite solid solution in high temperature magmatic hydrothermal systems. Rpt. GSJ, high-temperature acid fluids and associated alteration and mineralization, vol. 277. In: the 3rd Symposium on Deep-Crust Fluids "High-Temperature Acid Fluids and Associated Alteration and Mineralization" proceeding, pp. 35-37.

Browne PRL, Lawless JV (2001) Characteristics of hydrothermal eruptions, with examples from New Zealand and elsewhere: *Earth-Science Reviews*. doi: 10.1016/S0012-8252(00)00030-1.

Center Volcanology and Hazard Mitigation (2016) Database of volcanoes in Indonesia; CVGHM Report.

Chatterjee ND, Johannes W, Leistner H (1984) The system CaO-Al₂O₃-SiO₂-H₂O: new phase equilibria data, some calculated phase relations, and their petrological applications. *Contribution Mineralogy Petrology*. doi: [10.1007/BF00371407](https://doi.org/10.1007/BF00371407).

Christenson BW, Reyes AG, Young R, Moebis A, Sherburn S, Cole-Baker J (2010) Cyclic processes and factors leading to phreatic eruption events: insights from the 25 September 2007 eruption through Ruapehu Crater Lake, New Zealand. *Journal Volcanology and Geothermal Research*. doi: 10.1016/j.jvolgeores.2010.01.008

Dong G, Morrison G, Jaireth S (1995) Quartz texture in epithermal veins, Queensland – classification, origin, and implication. *Economic Geology*. doi: 10.2113/gsecongeo.90.6.1841.

Fournier RO (1985) The behavior of silica in hydrothermal solution. In: *Review in economic geology*. doi: [10.5382/Rev.02.03](https://doi.org/10.5382/Rev.02.03).

Giggenbach WF (1997) The origin and evolution of fluids in magmatic-hydrothermal systems. In: *Geochemistry of hydrothermal ore deposit 3rd ed.*, Barnes, H. L., ed., Wiley, New York.

Hara J, Tsuchiya N (2009) Chemical modification of pyroclastic rock by hot water: an experimental investigation of mass transport at the fluid-solid interface. *Geofluids*. 9: 24-38.

Hedenquist JW, Arribas A Jr, Reynolds TJ (1998) Evolution of an intrusion-centered hydrothermal system: Far Southeast-Lepanto porphyry and epithermal Cu–Au deposits, Philippines. *Economic Geology*. doi:10.2113/gsecongeo.93.4.373.

Hedenquist JW, Henley RW (1985) Hydrothermal eruptions in the Waiotapu geothermal system, New Zealand; their origin, associated breccias, and relation to precious metal mineralization. *Economic Geology*. 80: 1640-1668.

Hedenquist JW, Lowenstern JB (1994), The role of magmas in the formation of hydrothermal ore deposits. *Nature*. 370: 519-527.

Hedenquist JW, Taran Y (2013) Modeling the formation of advanced argillic lithocaps: volcanic vapor condensation above porphyry intrusions. *Economic Geology*. doi:10.2113/econgeo.108.7.1523.

Hemley JJ, Montoya JW, Marinenko JW, Luce RW (1980) Equilibria in the System of Al_2O_3 - SiO_2 - H_2O and Some General Implications for Alteration/Mineralization Processes. *Economic Geology*. 75: 210-228.

Hochstein MP, Sudarman S (2015) Indonesian volcanic geothermal systems; Proceeding World Geothermal Congress 2015, Melbourne, Australia.

Imai A, Geshi N, Shimano T, Nakada S (2007) Implication of the temporal sulphur isotopic variation during the 2000 eruption of Miyakejima Volcano, Japan. *Island Arc*. 16: 83-92.

Imura T, Minami Y, Ohba T, Matsumoto A, Arribas Jr A, and Nakagawa M (2019) Hydrothermal aluminum-phosphate-sulfates in Ash from the 2014 hydrothermal eruption at Ontake Volcano, Central Honshu, Japan. doi: 10.3390/min9080462

Ikehata K, Maruoka T (2016) Sulfur isotopic characteristics of volcanic products from September 2014 Mount Ontake eruption, Japan. *Earth Planets Space*. doi: 10.1186/s40623-016-0496-z

Ikehata, K, Maruoka K (2019) Sulfur isotopic systematics during the October 2017 eruption of the Shinmoe-dake volcano, Japan. *Journal Applied Geochemistry*. doi: 10.1016/j.apgeochem.2019.01.009

John DA, Sisson TW, Breit GN, Rye RO, Vallance JW (2008) Characteristics, extent and origin of hydrothermal alteration at Mount Rainier Volcano, Cascades Arc, USA: Implications for debris-flow hazards and mineral deposits. *Journal of Volcanology and Geothermal Research*. doi: 10.1016/j.volgeo.2008.04.004

Kartadinata MN, Okuno M, Nakamura T, Kobayashi T (2002) Eruptive history of Tangkuban Parahu Volcano, West Java, Indonesia: A preliminary report. *Journal of Geography*, 111: 404-409.

Kartadinata MN (2005) Tephrochronological study on eruptive history of Sunda-Tangkuban Perahu volcanic complex, West Java, Indonesia. Doctoral Dissertation, Kagoshima University.

Kusakabe M, Mizutani Y, Kometani M (1982) A Preliminary Stable Isotope Study of Volcanic Ashes Discharged by the 1979 Eruption of Ontake Volcano, Nagano, Japan. *Bulletin of Volcanology*. 43: 204-209.

Kusumadinata K (1979). Database of volcanoes in Indonesia. Center Volcanology and Hazard Mitigation.

Laetsch T, Downs R (2006) Software for identification and refinement of cell parameter from powder diffraction data of minerals using the RRUFF Project and American Mineralogist Crystal Structure Databases. the 19th general meeting of the International Mineralogical Association, Kobe, Japan.

Landis GP, Rye RO (2005) Characterization of gas chemistry and noble-gas isotope ratios of inclusion fluids in magmatic-hydrothermal and magmatic-steam alunite. *Chemical Geology*. 215: 155-184.

Li G, Peacor DR, Essene EJ, Brosnahan DR, Beane RE (1992) Walthierite $Ba_{0.5}\square_{0.5}Al_3(SO_4)_2(OH)_6$ and huangite $Ca_{0.5}\square_{0.5}Al_3(SO_4)_2(OH)_6$, two new minerals of the alunite group from the Coquimbo region, Chile. *American Mineralogist* 77:1275-1284.

Lowenstern JB, van Hinsbern V, Berlo K, Liesegang M, Iacovino K, Bindeman IN, Wrigth HM (2018) Opal-A in glassy pumice, acid alteration, and the 1817 phreatomagmatic eruption at Kawah Ijen (Java), Indonesia. *Frontiers in Earth Science*. doi: 10.3389/feart.2018.00011.

Manalo PC, Imai A, Subang LL, Santos MC, Yanagi K, Takahashi R, and Blamey NJF (2018) Mineralization of the Northwest Quartz-Pyrite-Gold Veins: Implications for Multiple Mineralization Events at Lepanto, Mankayan Mineral District, Northern Luzon, Philippines. *Economic Geology*. doi:10.5382/econgeo.2018.4606

Mastin, LG (1995), Thermodynamics of gas and steam-blast eruptions. *Bulletin Volcanology*. 57: 85-98.

Miyagi I, Geshi N, Hamasaki S, Oikawa T, Tomiya A (2020) Heat source of the 2014 phreatic eruption of Mount Ontake, Japan; *Journal Volcanology and Geothermal Research*. doi: 10.1007/S00445-020-1358-x

Minami Y, Imura T, Hayashi S, and Ohba T (2016) Mineralogical study on volcanic ash of the eruption on September 27, 2014 at Ontake volcano, central Japan: correlation with porphyry copper systems. *Earth, Planets and Space*. doi: 10.1186/s40623-016-0440-2.

Nasution A, Kartadinata MN, Sutamingsih E, Hadisantono R, Kadarsetia E, Kobayashi, T, Siregar D (2004) Geology, age dating, and geochemistry of the Tangkuban Parahu Geothermal Area, West Java, Indonesia. *Journal of the Geothermal Research Society of Japan*. doi: 10.11367/grsj1979.26.285

Nogami K, Yoshida M (1993) Leaching process of rock forming components through acidic alteration. *The Chemical Society of Japan*. 3: 251-258. (In Japanese with English abstract)

Nogami K, Yoshida M (1995) Leaching rates of rock-forming components through acidic alteration. *Journal of Volcanology and Geothermal Research*. 65: 289-314.

Ohba T, Taniguchi H, Miyamoto T, Hayashi S, Hasenaka T (2007) Mud plumbing system of an isolated phreatic eruption at Akita Yakeyama volcano, northern Honshu, Japan. [Journal of Volcanology and Geothermal Research](#). doi: 10.1016/j.jvolgeores.2006.11.001.

- Ohmoto H, Rye RO (1979) *Isotopes of Sulfur and Carbon*. In: *Geochemistry of hydrothermal ore deposit* 2nd ed. Barnes HL, Wiley, New York.
- Ohmoto, H, Goldhaber MB (1997), *Sulfur and Carbon Isotopes*. In *Geochemistry of hydrothermal ore deposit* 3rd ed. Barnes HL, Wiley, New York.
- Pardo N, Cronin SJ, Nemeth K, Brenna M, Schipper CI, Breard E, White JDL, Procter J, Stewart B, Agustin-Flores J, Moebis A, Zernack A, Kerezturi G, Lube G, Auer A, Neall V, Wallace C (2014) Perils in distinguishing phreatic from phreatomagmatic ash: insights into the eruption mechanisms of the 6 August 2012 Mt. Tongariro eruption, New Zealand. *Journal of Volcanology and Geothermal Research*. doi: 10.1016/j.jvolgeores.2014.05.001
- Rye RO, Bethke PM, Wasserman MD (1992) The stable isotope geochemistry of acid sulfate alteration. *Economic Geology*. doi: 10.2113/gsecongeo.87.2.225.
- Rye RO (1993) The evolution of magmatic fluids in the epithermal environment: the stable isotope perspective. *Economic Geology*. doi: 10.2113/gsecongeo.88.3.733.
- Rye RO (2005) A review of the stable-isotope geochemistry of sulfate minerals selected igneous environments and related hydrothermal systems. *Chemical Geology*. doi: 10.1016/j.chemgeo.2004.06.034.
- Rodríguez A, van Bergen MJ (2017) Superficial alteration mineralogy in active volcanic systems: an example of Poás volcano, Costa Rica. *Journal of Volcanology and Geothermal*. doi: 10.1016/j.jvolgeores.2017.04.006
- Sakai H (1968) Isotopic properties of sulfur compounds in hydrothermal processes. *Journal of Geochemical*. 2: 29-49.
- Scher S, Williams-Jones A, Williams-Jones G (2013) Fumarolic activity, acid-sulfate alteration, and high sulfidation epithermal precious metal mineralization in the Crater of Kawah Ijen Volcano, Java, Indonesia. *Economic Geology*. doi:10.2113/econgeo.108.5.1099.
- Sjarifudin MZ, Pratomo I, and Rakimin P (1984) Report the petro-chemistry of Sunda and Tangkuban Parahu Volcanoes. Center Volcanological and Hazard Mitigation.
- Sillitoe RH (2010) Porphyry copper system. *Economic Geology*. doi: 10.2113/gsecongeo.105.1.3
- Stoffregen RE and Alpers CN (1987) Woodhouseite and svanbergite in hydrothermal ore deposits: Products of apatite destruction during advanced argillic alteration. *Canadian Mineralogist*. 25: 201-211.
- Sunardi E, Kimura J (1998) Temporal chemical variation in late cenozoic volcanic rocks around Bandung Basin, West Java, Indonesia. *Journal Mineralogy, Petrology, and Economic Geology*. 93: 103-128.

- Sriwarno T (1984) Report of the geochemical investigation of Tangkuban Parahu Volcano. Center Volcanological and Hazard Mitigation.
- Sunardi E, Kimura J (1998) Temporal chemical variation in late cenozoic volcanic rocks around Bandung Basin, West Java, Indonesia. *Journal Mineralogy, Petrology, Economic Geology* 93: 103-128.
- Suryo I (1981) Report of the volcanic activity in Indonesia for the period 1961-1963. *Bulletin Volcanological Survey Indonesia* 104: 116.
- Suryo I (1985) Report of the volcanic activity in Indonesia for the period 1964-1970. *Bulletin Volcanological Survey Indonesia* 106: 150.
- Syahidan AA, Suryantini A, Susanto, Nurdiana A (2015) Hydrothermal alteration study of Tangkuban Parahu Craters, and its implication to geothermal conceptual model. *Proceeding Indonesia International Geothermal Convention and Exhibition*.
- Takahashi R, Yahata M (2018) Effects of subvolcanic hydrothermal systems on edifice collapses and phreatic eruptions at Tokachidake volcano, Japan. *Journal Volcanology and Geothermal Research*. doi: 10.1016/j.jvolgeores.2018.01.014
- Van Hinsberg V, Berlo K, van Bergen M, Williams-Jones A (2010) Extreme alteration by hyperacidic brines at Kawah Ijen volcano, East Java, Indonesia: I. Textural and mineralogical imprint. *Journal Volcanology and Geothermal Research*. doi:10.1029/2012GC004192
- Watanabe Y, Aoki M, Yamamoto K (1997) Geology, age, and style of advanced argillic alteration in the Kobui Area, Southwestern Hokkaido, Japan. *Resource Geology*. 47: 263-281.
- Watanabe Y, Hedenquist JW (2001) Mineralogical and stable isotope zonation at the surface over the El Salvador porphyry Cu deposit, Chile. *Economic Geology*. doi:10.2113/96.8.1775.
- Watanabe Y, Ohta E (2005) Polymetallic Pb-Zn-Ag-In Toyoha Deposit; geology, style, genesis, and exploration. Institute for Geo-Resources and Environment, AIST.
- Wasserman MD, Rye RO, Bethke PM, Arribas Jr A (1992) Methods for separation and total stable isotope analysis of alunite. U.S. Geological Survey Open File Report. 20: 92-9. <https://pubs.er.usgs.gov/publication/ofr929>.
- Wohletz K, Heiken G (1992) *Volcanology and Geothermal Energy*. University of California, Berkeley.
- Yanagisawa F, Sakai H (1983) Thermal decomposition of barium sulfate-vanadium pentoxide-silica glass mixtures for preparation of sulfur dioxide in sulfur isotope ratio measurements. *Analytical Chemistry*. doi:10.1021/ac00257a046.

Zimbelman DR, Rye RO, Breit GN (2005) Origin of secondary minerals on active andesitic stratovolcanoes. doi: 10/1016/j.chemgeo.2004.06.056

Tables

Due to technical limitations, table 1, 2 is only available as a download in the Supplemental Files section.

Figures

Figure 1

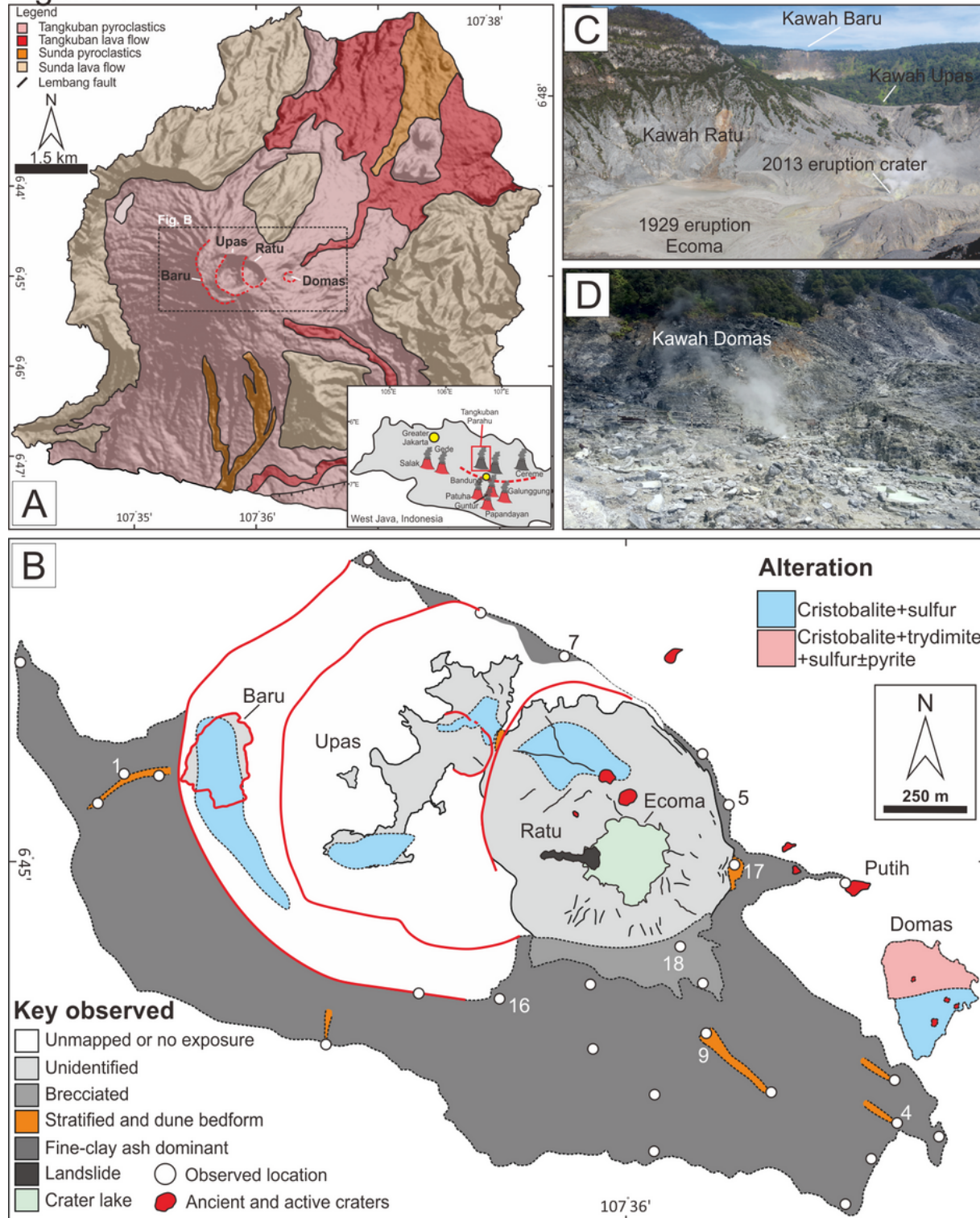


Figure 1

A) Map showing general geological information (modified after Nasution et al., 2004) and location of Mt. Tangkuban Parahu in West Java, Indonesia. B) Map showing the geological distribution of eruptive products at the proximal area, in combination with hydrothermal zonation within the active craters from Syahidan et al. (2015). C) Photograph showing most active craters of Ratu at the summit of the volcano,

including the Ecoma (1929 eruption) and 2013 eruption craters. D) Photograph showing the hydrothermal manifestation (e.g., fumarole; hot pools) at Domas Crater.

Figure 2

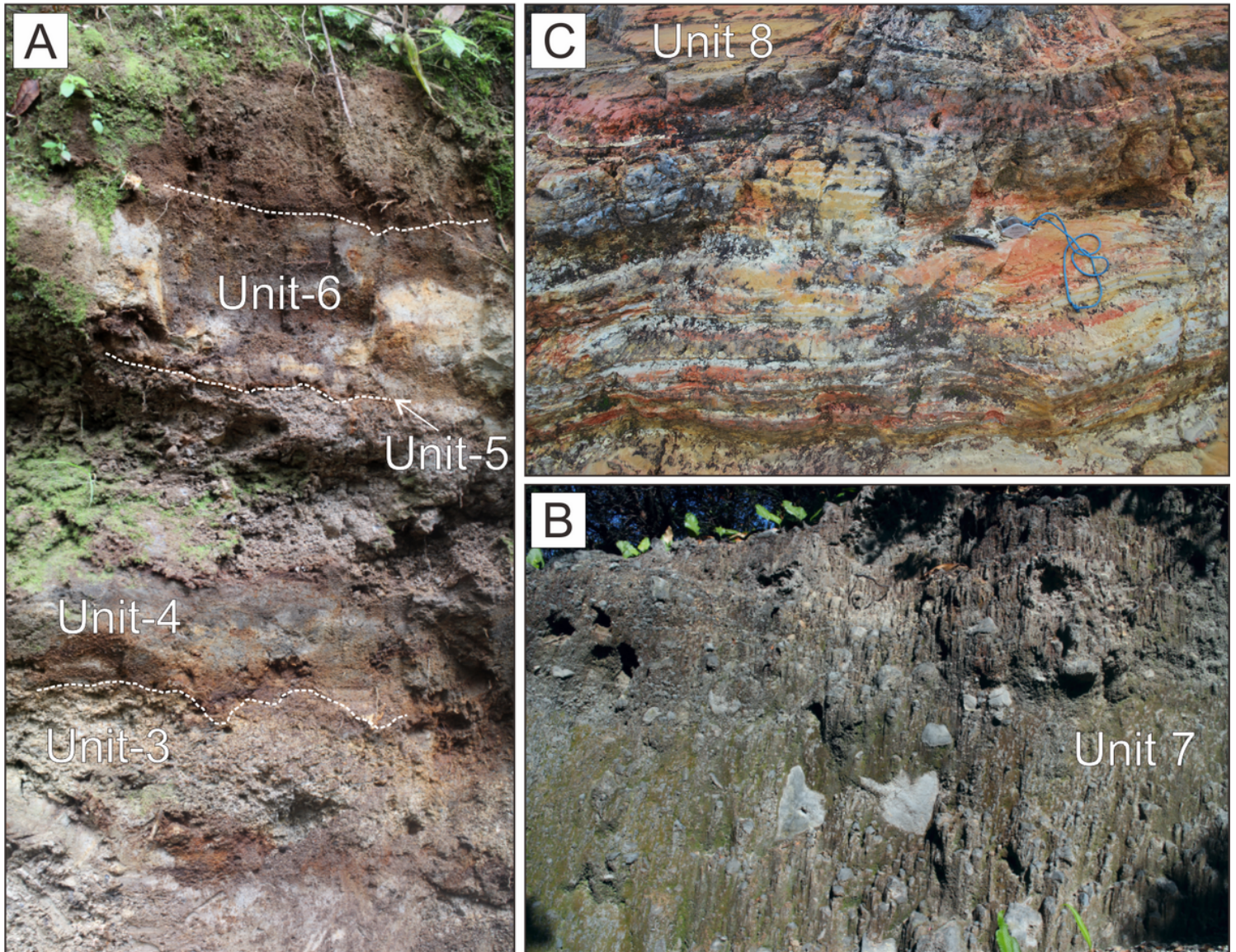


Figure 2

Photographs are showing outcrop of the analyzed samples at Tangkuban Parahu, Indonesia. A) White to grey volcanic products are characteristics of proximal tephra succession. Units were divided by the presence of very-thin paleosols (>5 cm) and continuous successive volcanic products. B) Thicknesses range from laminae (>1cm) to bedding. C) The upper portion of studied stratigraphy (e.g., Unit 7-10) is predominantly composed of poorly sorted, heterolithic, and matrix-supported, whereas the lower stratigraphic section consisting mainly of well-sorted fine-ash to lapilli deposits.

Figure 3

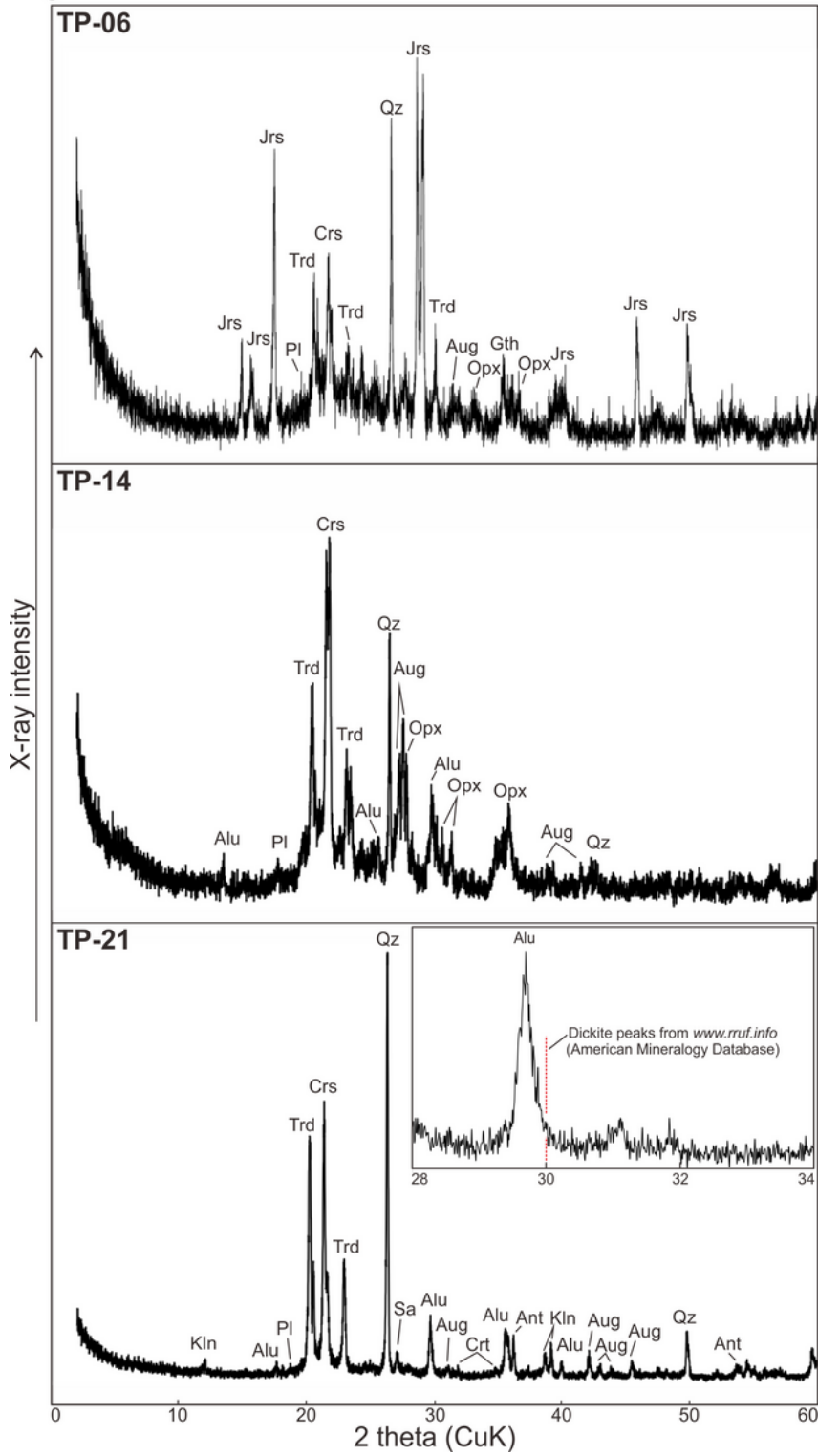


Figure 3

X-ray diffractograms show interpretation of mineral phases in representative volcanic products (TP-06, TP-14, and TP-21).

were found in several volcanic products (Unit 1, 2, 4, and 6). Hydrothermal minerals are predominantly comprise of a large number of silica minerals associated with alunite, alunite±kaolinite, and alunite+jarosite+goethite together with partly altered glassy magmatic pyroclasts.

Figure 5

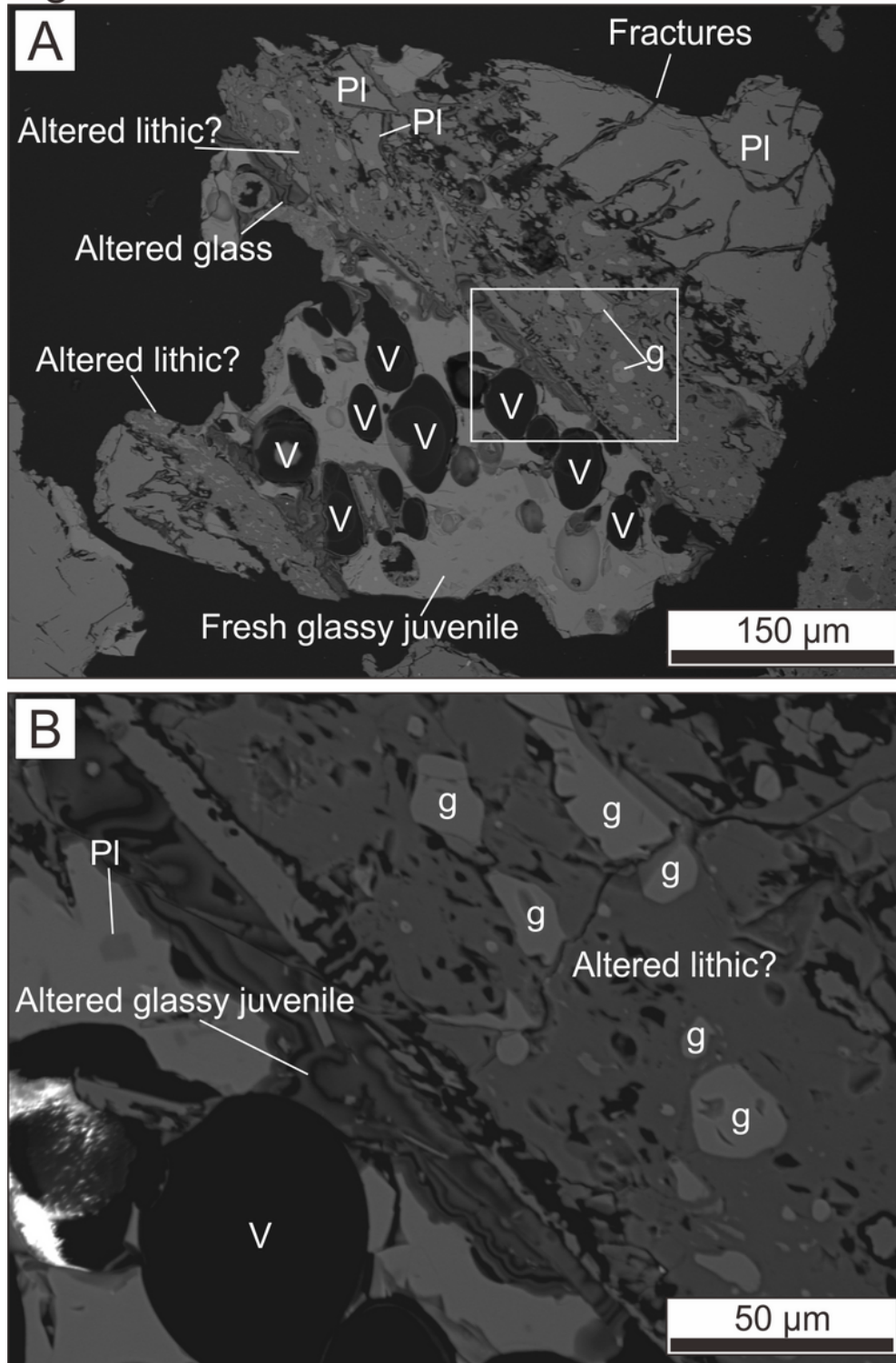


Figure 5

Backscattered electron images showing the example of partly altered glassy magmatic juveniles in Unit 3 and 4. A) Partly altered glassy magmatic juveniles mainly composed of plagioclase, clinopyroxene, and

interstitial glass along with vesicle and bubble textures. Most of the magmatic minerals (e.g., plagioclase) are fractured and possibly filled by hydrothermally altered minerals (e.g., silica). B) BSE image shows colloform-like banding of thinly altered interstitial glass in contact with lithics. Hydrothermally altered lithics are occurring as a replacement of glassy groundmass as well as microlite of magmatic minerals.

Figure 6

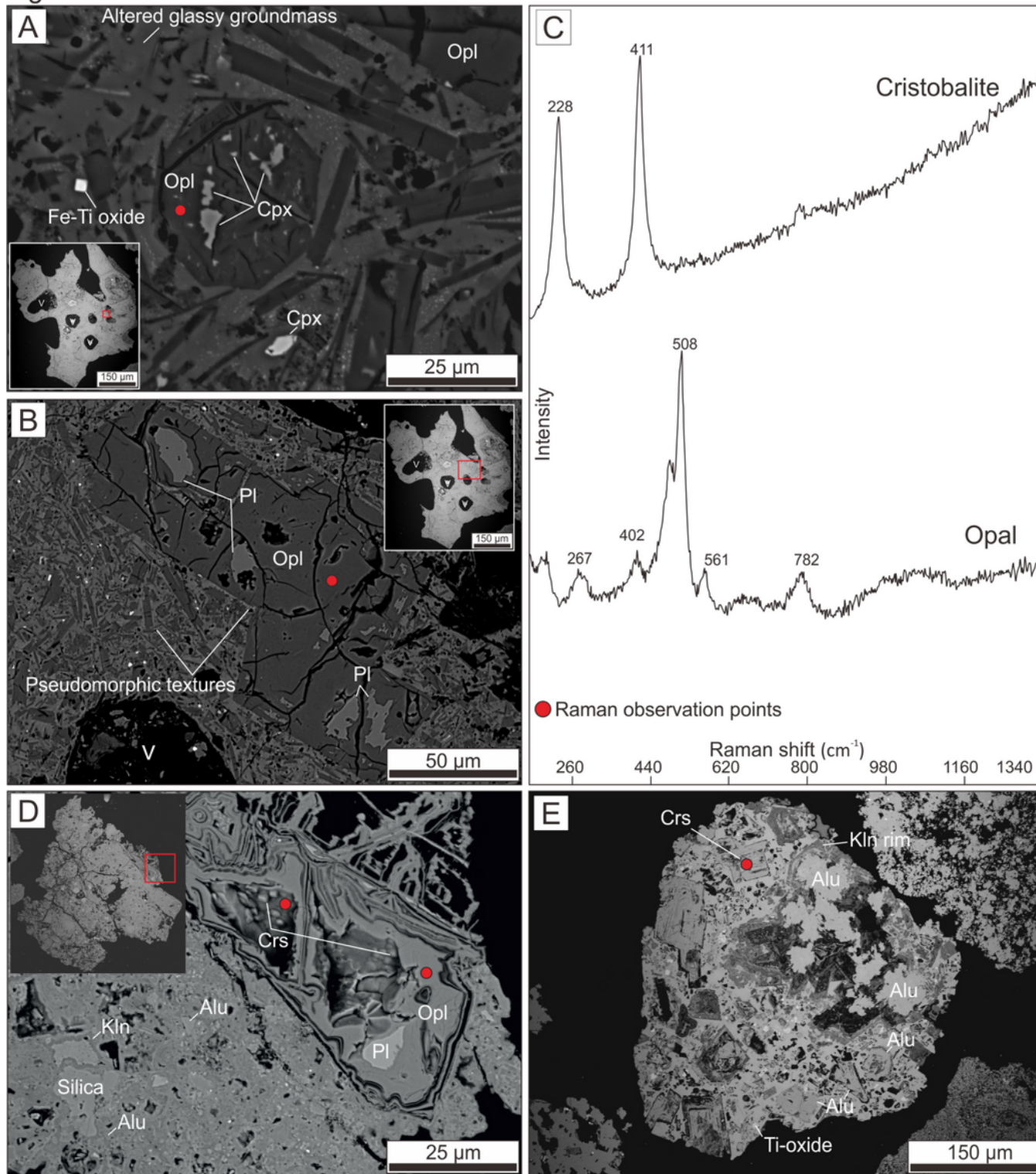


Figure 6

Backscattered electron images showing the textural features of opal and opal-cristobalite±alunite±kaolinite in ash particles, including the Raman Spectral from selected point analyses from several ash particles. A) Opal alteration was found on vesiculated ash particles. Vesicular textures were filled with silica minerals. Magmatic minerals were replaced by opal, where the relict of magmatic minerals (A, B) remains at the core of crystals. C). Graph showing the two representatives Raman spectrum of cristobalite and opal in ash particles (B, D). D) BSE image shows opal-cristobalite after plagioclase, whereas silica-alunite±kaolinite occurs as a groundmass alteration. F) Opal-cristobalite-silica-alunite sporadically replaced the magmatic minerals in dense ash particles. Most of the hydrothermal minerals occur as pseudomorphic textures.

Figure 7

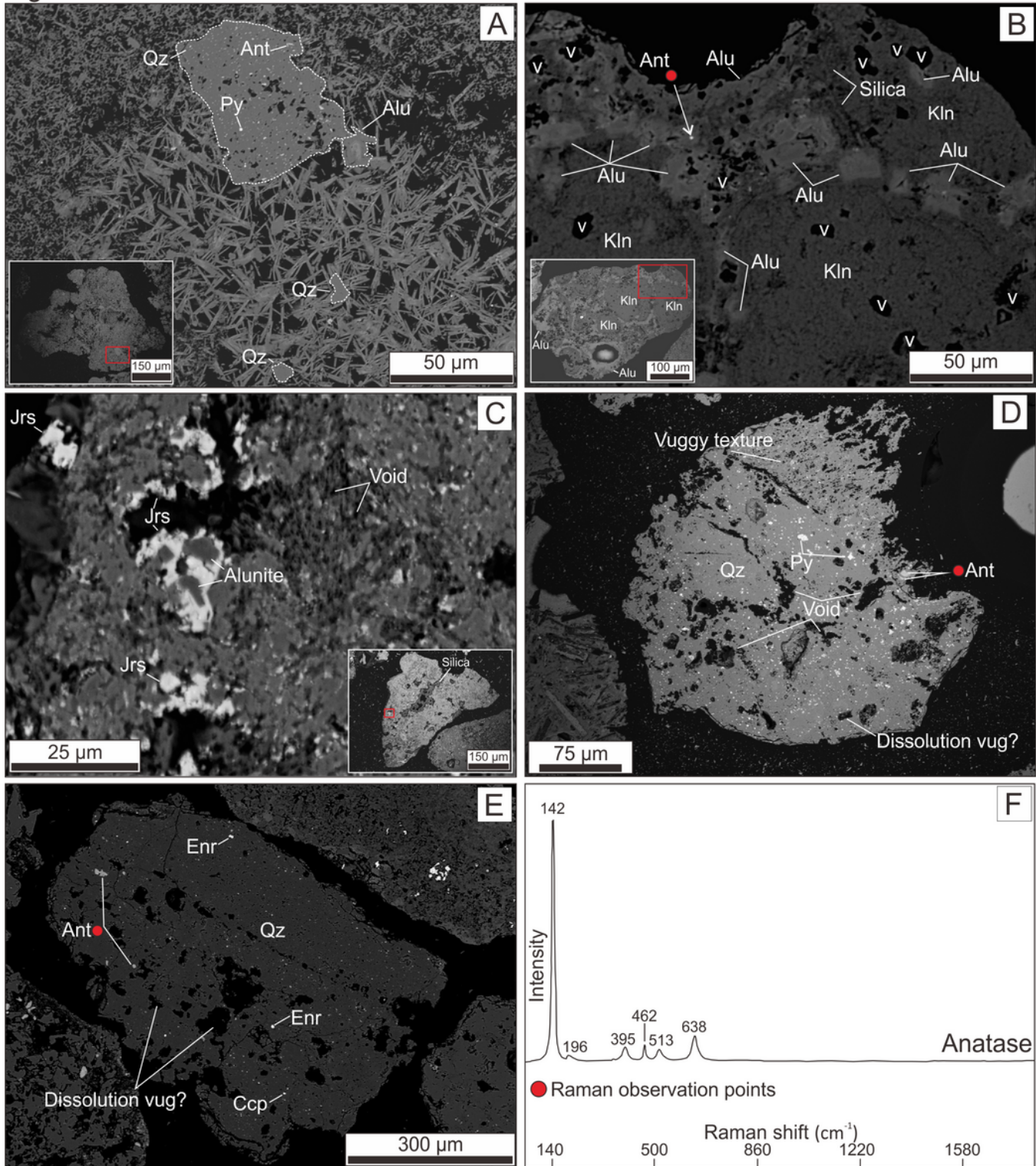


Figure 7

Backscattered electron images showing the textural features of quartz-alunite±kaolinite, alunite-jarosite, and quartz alteration assemblages in ash particles. A) Quartz-alunite±kaolinite alteration is also associated with a cluster of quartz±pyrite±anatase assemblage along with pervasive quartz alteration. B) Alunite occurs as equant crystal shape, which is associated with circular kaolinite crystal clusters, anatase, and silica mineral. C) Alunite-jarosite was found in the subangular to subrounded ash particles.

Jarosite occurs as alunite-jarosite intergrown texture. Both minerals are associated with silica minerals that mainly occurs as pore-filling minerals. D) BSE image shows a pervasive quartz alteration of subangular to subrounded ash particles. A vuggy texture develops at the edge of ash particles, where the anhedral and elongated shape pyrite filled up the pore space of vuggy textures. E) BSE image shows an example of ash particle with pervasive quartz alteration. Quartz alteration is associated with anatase, enargite, chalcopyrite, titanomagnetite, and magnetite. F) Graph showing the representative of Raman spectrum of anatase in alunite and quartz alteration.

Figure 8

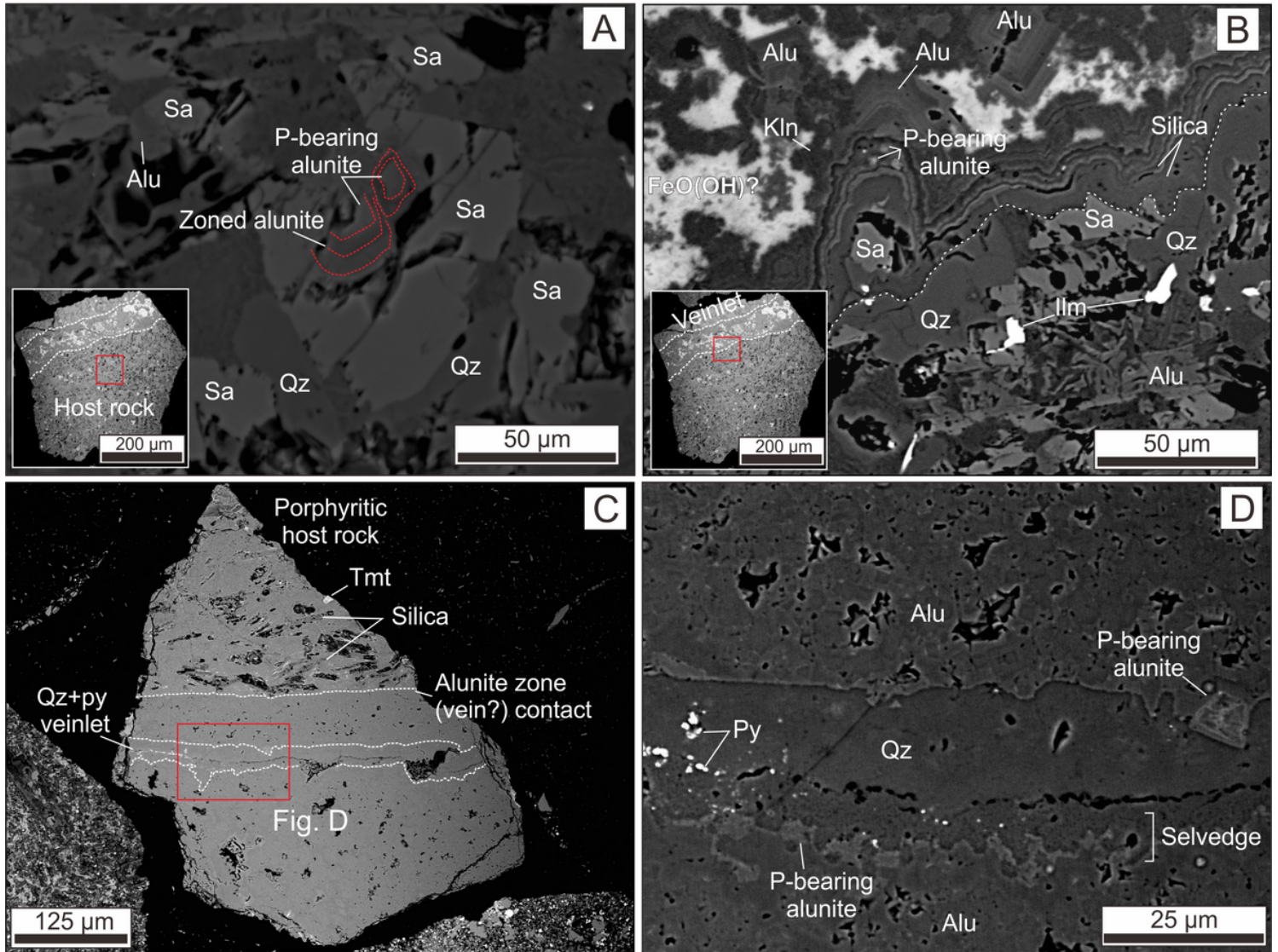


Figure 8

Backscattered electron image showing two examples of the feeder veinlet in different hosts of volcanic rock. A) Host rock mineralogy is mainly composed of euhedral to anhedral quartz, sanidine, ilmenite, and titanomagnetite. Most of the mineral was intensely altered into a mixture of silica minerals as well as alunite and P-bearing alunite. B) Veinlet mineralogy consists of silica, P-bearing alunite, alunite, kaolinite, goethite, and a small number of Ti-oxide (anatase). BSE image band also shows the colloform-like banding of early-stage veinlet deposition, which is located close in contact with holocrystalline-porphyritic

textured hypabyssal rocks. C) The second veinlet consists of quartz and centreline pyrite crystal bleps within the cluster of alunite crystals. P-bearing alunite mainly occurs along the rim of quartz-pyrite veinlet. Figure 9

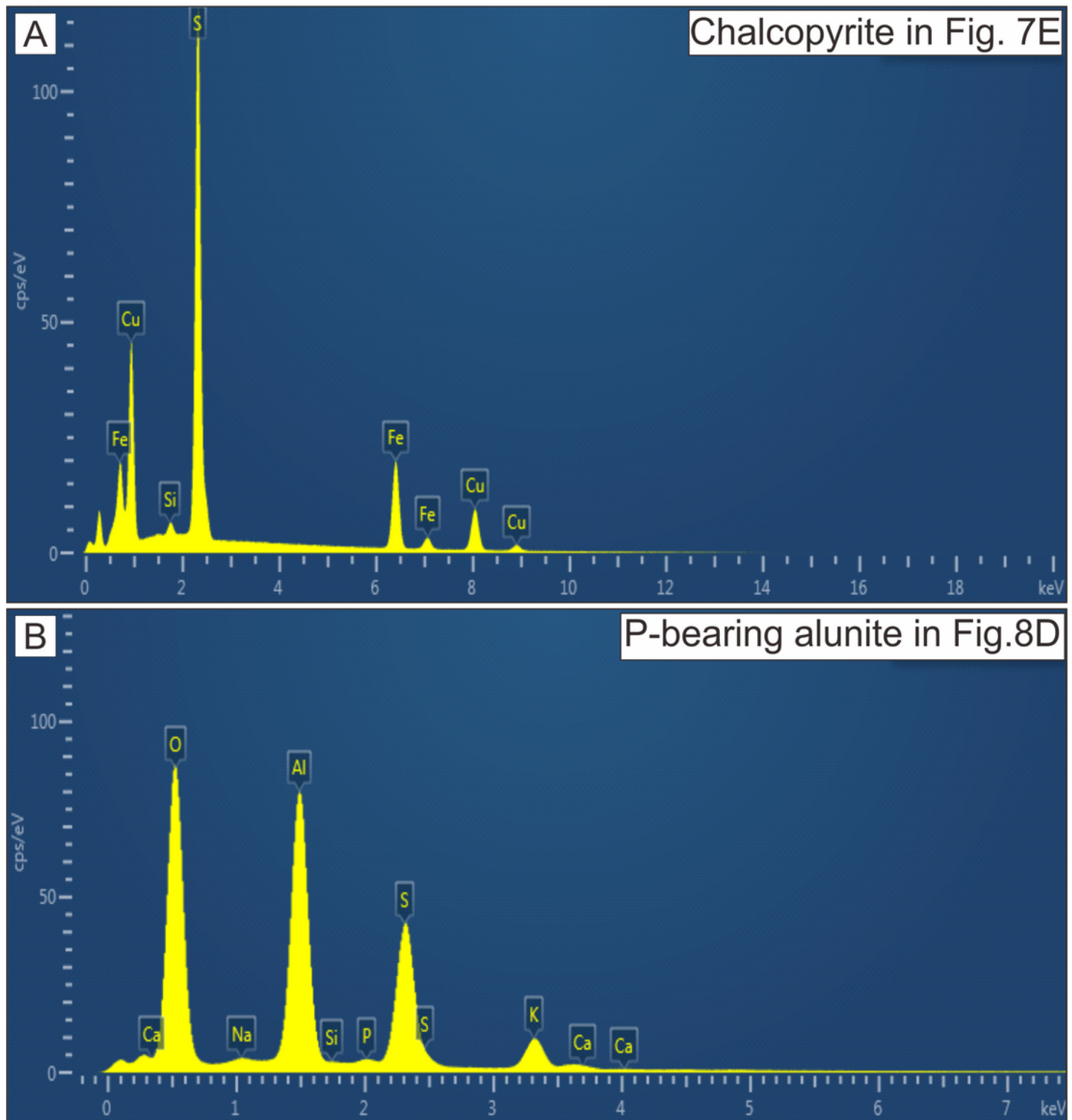


Figure 9

Graphs showing the elemental spectrum of EDS analysis. A) EDS spectrum displays the analytical results for the occurrence of chalcopyrite in Fig. 7E. It should be noted that Si spectrum represents the quartz x-

ray spectrum on host alteration mineral. B) The EDS spectrum shows the presence of P-bearing alunite in alunite vein (Fig. 8D).
 Figure 10

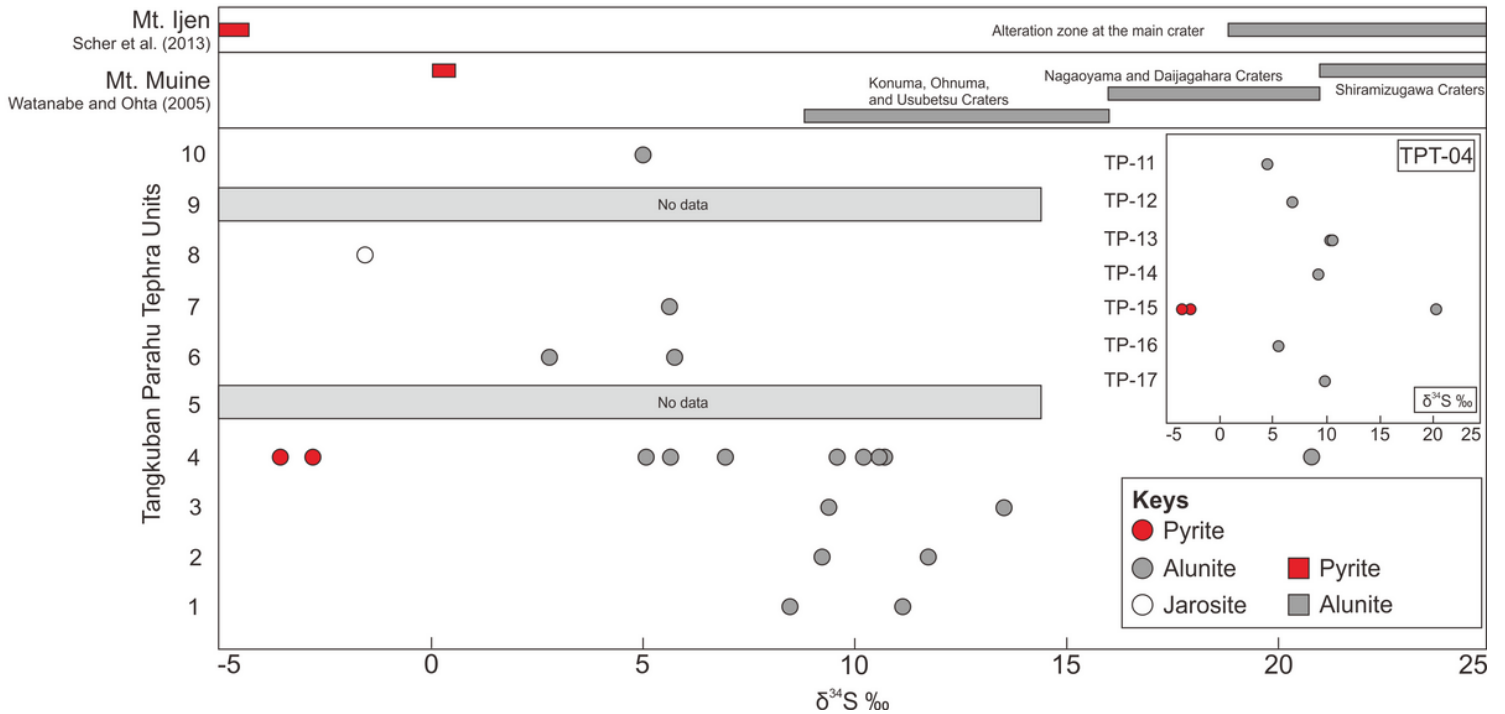


Figure 10

Graph showing the plot of the sulfur isotopic composition of alunite, pyrite, and jarosite against the studied stratigraphic unit in Angkasa et al., 2019. The $\delta^{34}\text{S}$ values are compared to $\delta^{34}\text{S}$ values from sulfide and sulfate samples at Mt. Muine (Watanabe and Ohta, 2005) and Kawah Ijen (Scher et al., 2013).

Supplementary Files

This is a list of supplementary files associated with this preprint. Click to download.

- [Abstract.png](#)
- [Table1.xls](#)
- [Table2.xlsx](#)